Research Article | Open Access

Soft Science

Lu *et al. Soft Sci.* **2026**, *6*, 100 **DOI:**10.20517/ss.2026.177

Flexible and oxidation-resistant graphene@SiC nanofiber fabrics

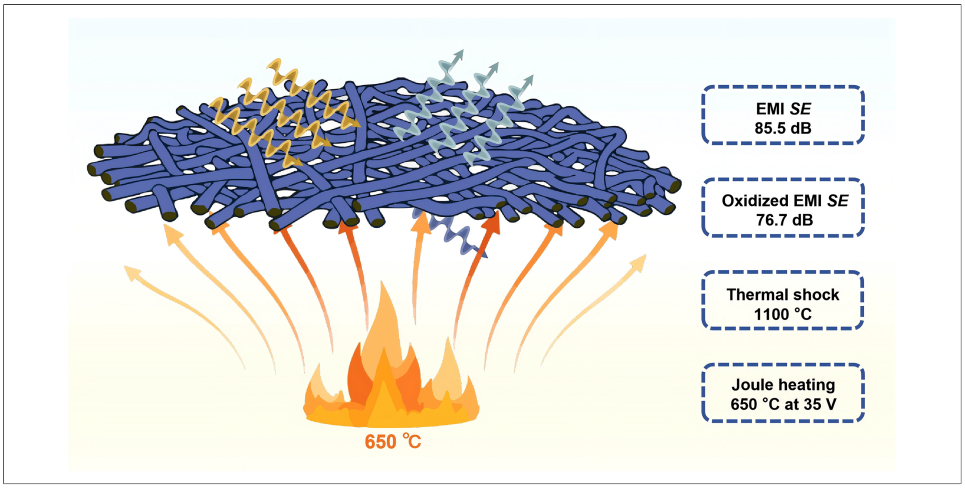
Shuai Lu[1,2,3], Zhanpo Han[2,4], Chang Shu[2], Zhiyao Zheng[2], Zhijie Zhou[2,5], Yifan Yao[2,6], Yi Han[7,*], Xinxin Jin[1,*], Zheng Li[2,*]

Keywords:
Graphene@SiC nanofiber fabrics, coaxial electrospinning, electromagnetic interference shielding, high-temperature oxidation resistance, Joule heating

Citation: Lu, S.; Han, Z.; Shu, C.; Zheng, Z.; Zhou, Z.; Yao, Y.; Han, Y.; Jin, X.; Li, Z. Flexible and oxidation-resistant graphene@SiC nanofiber fabrics. *Soft Sci.* **2026**, *6*, 100. https://dx.doi.org/10.20517/ss.2026.177

Received: 2 Jul 2026
First Decision: 31 Jul 2026
Revised: 14 Sep 2026
Accepted: 16 Sep 2026
Published: 9 Nov 2026

Academic Editor:
Mazeyar Parvinzadeh Gashti
Copy Editor:
Pei-Yun Wang
Production Editor:
Pei-Yun Wang



Abstract

Carbon-based macroscopic architectures hold immense potential in flexible electronics owing to their low density and exceptional electrical conductivity. However, their susceptibility to oxidative degradation at elevated temperatures severely restricts their deployment in extreme environments. Here, we report the design of flexible graphene@silicon carbide core-shell nanofiber fabrics (G@SiC NFFs) fabricated via coaxial electrospinning and sequential thermal processing. The resulting hierarchical structure features a highly conductive graphene nanofiber core coaxially shielded by an oxidation-resistant SiC shell, seamlessly integrated via a robust heterointerface. Benefiting from their unique architecture, 20 wt% polycarbosilane-derived G@SiC NFFs achieved a frequency-averaged X-band electromagnetic interference (EMI) shielding effectiveness exceeding

[1]Shao Xing Institute of Technology, School of Pharmacy and Health Sciences, Shaoxing Institute of Technology, Shaoxing 312000, Zhejiang, China.
[2]ZJU-Hangzhou Global Scientific and Technological Innovation Center, Key Laboratory for Biomedical Engineering of Education Ministry, Zhejiang Key Laboratory of Intelligent Sensing Technology and Advanced Medical Instrument, College of Biomedical Engineering & Instrument Science, Zhejiang University, Hangzhou 310027, Zhejiang, China.
[3]School of Materials Science and Chemical Engineering, Harbin University of Science and Technology, Harbin 150040, Heilongjiang, China.
[4]National Key Laboratory of Science and Technology on Advanced Composites in Special Environments, Harbin Institute of Technology, Harbin 150080, Heilongjiang, China.
[5]State Key Laboratory of Flexible Electronics (LoFE) & Jiangsu Key Laboratory of Smart Biomaterials and Theranostic Technology, Institute of Advanced Materials (IAM), Nanjing University of Posts and Telecommunications, Nanjing 210023, Jiangsu, China.
[6]College of Integrated Circuits, Zhejiang University, Hangzhou 311200, Zhejiang, China.
[7]Hangzhou Gaoxi Technology Co., Ltd, Hangzhou 311113, Zhejiang, China.

***Correspondence to:** Prof. Zheng Li, ZJU-Hangzhou Global Scientific and Technological Innovation Center, Key Laboratory for Biomedical Engineering of Education Ministry, Zhejiang Key Laboratory of Intelligent Sensing Technology and Advanced Medical Instrument, College of Biomedical Engineering & Instrument Science, Zhejiang University, Hangzhou 310027, Zhejiang, China. E-mail: li.zheng@zju.edu.cn;

Prof. Xinxin Jin, Shao Xing Institute of Technology, School of Pharmacy and Health Sciences, Shaoxing Institute of Technology, Shaoxing 312000, Zhejiang, China. E-mail: jinxinxin@zsit.edu.cn; Dr. Yi Han, Hangzhou Gaoxi Technology Co., Ltd, Hangzhou 311113, Zhejiang, China. E-mail: firehuo@aliyun.com

80 dB at thicknesses of approximately 85-95 μm. A representative sample with a thickness of approximately 80 μm exhibited a shielding effectiveness of 85.5 dB and retained 76.7 dB after oxidation in air at 650 °C for 1 h. Remarkably, the fabrics exhibit robust electrothermal stability during prolonged exposure to an alcohol-lamp flame at 650 °C and thermal shock using an alcohol-torch flame at 1,100 °C, while also enabling reliable Joule heating up to 650 °C under ambient conditions. This work presents a strategy for developing lightweight and thermally resilient carbon-based electronics, paving the way for high-temperature EMI shielding and related extreme-environment applications.

INTRODUCTION

With the rapid development of aerospace electronics toward lightweight, flexible, and highly integrated systems, electromagnetic interference (EMI) has become a critical threat to device reliability and signal fidelity[1-3]. However, conventional shielding materials frequently fail in extreme high-temperature oxidative environments. To ensure reliable operation, an ideal shielding material must not only provide efficient electromagnetic attenuation but also retain its structural and electrical integrity under severe conditions, including prolonged oxygen exposure, abrupt thermal shocks, and drastic temperature fluctuations[4-10].

Although metallic shielding materials offer excellent electrical conductivity, their application in lightweight flexible electronics is fundamentally restricted by their high density, susceptibility to corrosion, and thermal expansion mismatch with deformable substrates[11,12]. Consequently, macroscopic architectures of carbon nanomaterials, particularly graphene assemblies, have emerged as promising lightweight alternatives because of their exceptional flexibility and robust conductive networks[1,2]. Specifically, ultrathin and porous graphene fabrics have demonstrated immense potential for highly efficient EMI shielding[3,4]. However, these carbon-based structures undergo rapid oxidative degradation at elevated temperatures, which severely compromises their long-term electrothermal stability in air[5-7]. This highlights a critical bottleneck: high initial conductivity alone is insufficient for durable EMI shielding in harsh environments; the conductive networks must be seamlessly protected by an oxidation-resistant barrier.

Efficient EMI shielding relies on the synergistic contributions of electrical conduction and dielectric dissipation[8,9]. A conductive core/ceramic shell architecture is well suited to this requirement. The conductive core ensures continuous carrier transport for ohmic loss, while the ceramic shell acts as an impenetrable barrier against thermal oxidation. Furthermore, the heterointerfaces between the core and shell can induce pronounced interfacial polarization and relaxation loss, substantially enhancing absorption-dominated shielding[10,11]. Recent work has demonstrated that dielectric-shell engineering can enhance electromagnetic-wave absorption in core-shell composites by modulating dielectric properties and interfacial polarization[12]. Recent advances have also integrated microwave absorption with photothermal conversion, thermal-energy storage, and thermoelectric cogeneration through interfacial engineering[13]. Previous studies have explored graphene-based textiles and related carbon/ceramic architectures for EMI shielding, Joule heating, sensing, and high-temperature stability, with the reported functional combinations varying among material systems. Silicon carbide (SiC)-coated carbon structures and ceramic nanofiber mats have primarily focused on oxidation-resistant EMI shielding at elevated temperatures[7,10]. More recently, Yang *et al.* reported a bioinspired C-SiC fibrous aerogel that combines thermal insulation, EMI shielding, and oxidation resistance at 1,000 °C[14]. However, maintaining electrical continuity in flexible carbon-based architectures under prolonged oxidative heating remains challenging. Guided by these considerations, we propose a

rationally designed architecture wherein a very thin oxidation-resistant SiC ceramic shell is coaxially integrated onto macroscopic fabric-like graphene networks[15-17]. This conformal encapsulation not only shields the internal graphene fiber core from oxidative ablation but also generates dense carbon/SiC heterointerfaces that amplify dielectric loss[14,15]. This core-shell strategy promises to preserve both the conductive percolation network and shielding efficiency in extreme thermal environments.

Here, we report the fabrication of flexible graphene@silicon carbide nanofiber fabrics (G@SiC NFFs) through a scalable coaxial electrospinning process followed by programmed thermal conversion. Benefiting from the seamless structural integration, the resulting G@SiC NFFs demonstrate remarkable electrothermal stability. They retain robust EMI shielding performance and show minimal electrical resistance variation even after prolonged oxidative heating at 650 °C. Furthermore, the fabrics enable reliable and voltage-programmable Joule heating up to 650 °C in air. This work establishes a core-shell nanofiber strategy for developing lightweight, thermally resilient, and flexible electronics, paving the way for advanced EMI shielding in extreme-environment applications.

EXPERIMENTAL

Materials

Aqueous graphene oxide (GO) dispersion, with an average lateral size of approximately 30 μm and an initial concentration of 10 mg·mL^{-1}, was purchased from Hangzhou Gaoxi Technology Co., Ltd. (Hangzhou, China). Polycarbosilane (PCS) was obtained from Suzhou Saifen Technology Co., Ltd. (Suzhou, China). Sodium polyacrylate (PAS), polyvinylpyrrolidone (PVP), and Triton X-100 were purchased from Macklin Biochemical Co., Ltd. (Shanghai, China). Hydroiodic acid, *N,N*-dimethylformamide (DMF), toluene, and absolute ethanol (analytical grade) were purchased from Sinopharm Chemical Reagent Co., Ltd. (Shanghai, China). All reagents were used as received without further purification. Deionized water was used throughout the experiments.

Preparation of precursor solutions

The commercial GO dispersion and PAS aqueous solution were concentrated to 20 mg·mL^{-1} before use. The GO5 core-spinning solution was prepared by mixing the GO dispersion, PAS solution, and Triton X-100 at a volume ratio of 1:1:0.1, yielding a GO concentration of approximately 9.52 mg·mL^{-1} (0.95 wt%). GO6 was prepared by changing the volume ratio of GO dispersion to PAS solution to 6:4 while maintaining the total volume of the two solutions and the Triton X-100 content; the corresponding mixing ratio was 1.2:0.8:0.1, yielding a GO concentration of approximately 11.43 mg·mL^{-1} (1.14 wt%). Both dispersions were filtered before use. Unless otherwise stated, GO5 was used as the baseline core solution for fabricating G@SiC NFFs.

The shell spinning solution was prepared by dissolving PCS and PVP in a toluene/DMF mixed solvent at a volume ratio of 7:3. The mixture was stirred at 25 °C and 120 rpm for 12 h to obtain a homogeneous solution. Unless otherwise specified, the baseline shell solution contained 20 wt% PCS and 6 wt% PVP, with the weight percentages calculated relative to the total mass of the shell spinning solution.

To investigate the influence of shell composition on coaxial electrospinning behavior and core-shell fiber formation, two shell-composition series were prepared. In the PCS-content series, the PVP content was fixed at 6 wt%, whereas the PCS content was varied from 10 to 40 wt%; the corresponding samples were denoted as GPCS10, GPCS15, GPCS20, GPCS25, GPCS30, GPCS35, and GPCS40, respectively. In the PVP-content series, the PCS content was fixed at 20 wt%, whereas the PVP content was varied from 2 to 8 wt%; the corresponding samples were denoted as GPVP2, GPVP4, GPVP6, and GPVP8, respectively. Additionally, formulations containing PVP at concentrations of 0, 2, 4, 6, 8, 10, and 12 wt% were prepared for the filament-drawing tests using the same procedure, with only the PVP concentration varied.

For clarity, pristine graphene nanofiber fabrics (GNFFs) without SiC encapsulation are denoted as GNFF, while SiC nanofiber fabrics without a graphene core are denoted as SiCNFF. The core-shell graphene@SiC nanofiber fabrics are denoted as G@SiC NFFs. Unless otherwise stated, G@SiC NFF refers to the baseline sample prepared using GO5 as the core solution and the shell formulation containing 20 wt% PCS and 6 wt% PVP. This baseline sample corresponds to GPCS20 in the PCS-content series and GPVP6 in the PVP-content series.

Fabrication of G@SiC NFFs

G@SiC NFFs were fabricated by coaxial electrospinning followed by sequential chemical reduction, oxidative crosslinking, and high-temperature ceramization[16,18]. The core and shell solutions were loaded into separate syringes and delivered through a coaxial spinneret with inner and outer needle diameters of 0.5 and 1.2 mm, respectively. During flow-rate optimization, the shell flow rate was maintained at 0.032 mL·min^{-1}, whereas the core flow rate was varied between 0.014 and 0.028 mL·min^{-1}, corresponding to shell-to-core flow-rate ratios of 1.14-2.28. For all subsequent experiments, the optimized shell and core flow rates were fixed at 0.032 and 0.018 mL·min^{-1}, respectively, corresponding to a shell-to-core flow-rate ratio of 1.78. Electrospinning was performed at 45-55 °C and 5%-15% relative humidity. The applied voltage and tip-to-collector distance were adjusted within 17-23 kV and 10-15 cm, respectively, to maintain a stable coaxial jet. The resulting nanofibers were collected on a high-speed rotating drum to form uniform fabrics.

The as-collected graphene oxide@polycarbosilane (GO@PCS) precursor fabrics were converted into G@SiC NFFs through a three-step post-treatment process. First, the precursor fabrics were reduced by hydroiodic acid vapor at 90 °C for 12 h. Second, the reduced fabrics were heated in air to 200 °C at 2 °C·min^{-1} and held for 2 h to induce oxidative crosslinking of PCS. Third, the crosslinked fabrics were transferred to a tube furnace and heated to 1,400 °C at 2 °C·min^{-1} under flowing Ar, then held for 2 h. After ceramization, the furnace was naturally cooled to room temperature under Ar.

Control samples were prepared for comparison. GNFFs were prepared by single-nozzle electrospinning of the GO/PAS solution, followed by HI vapor reduction and Ar annealing under the same conditions used for G@SiC NFFs. SiC nanofiber fabrics (SiCNFF) were prepared by single-nozzle electrospinning of the PCS/PVP shell solution, followed by air crosslinking and Ar ceramization under the same thermal conditions used for G@SiC NFFs.

Characterization

The morphology and microstructure of the NFFs were examined by field-emission scanning electron microscopy (FE-SEM, S400, Hitachi, Japan) at an accelerating voltage of 5 kV. The core-shell structure was characterized by transmission electron microscopy (TEM, JEM-2100F, JEOL, Japan) operated at 200 kV. Elemental distributions were analyzed by energy-dispersive X-ray spectroscopy (EDS) coupled with SEM or TEM. Cross sections of G@SiC NFFs were prepared and examined using a focused ion beam dual-beam microscope (FIB, DB550, CIQTEK, China).

The crystal structure and phase composition were analyzed by X-ray diffraction (XRD, D8 Advance, Bruker, Germany) using Cu Kα radiation. Raman spectroscopy (inVia Reflex, Renishaw, UK) was performed with a 532 nm laser to characterize the graphitic structure. The surface chemical composition and bonding states were investigated by X-ray photoelectron spectroscopy (XPS, K-Alpha+, Thermo Scientific, USA). All binding energies were calibrated using the C 1s peak at 284.8 eV as the reference. Fourier-transform infrared spectroscopy (FTIR, Nicolet iS50, Thermo Fisher Scientific, USA) was conducted in attenuated total reflectance mode to identify functional groups. Thermogravimetric analysis (TGA, Q500, TA Instruments, USA) was carried out in air at a heating rate of 10 °C·min^{-1} to evaluate thermal stability.

The electrical conductivity (σ) of the NFFs was measured at room temperature using an HPS2526 precision sheet resistance tester:

$$\sigma = \frac{L}{R \cdot w \cdot t} \tag{1}$$

where σ is the electrical conductivity ($S \cdot cm^{-1}$), R is the measured resistance (Ω), and L, w, and t represent the length (cm), width (cm), and thickness (cm) of the sample, respectively.

The Joule heating characteristics were monitored using a source meter (2450, Keithley Instruments, USA) and an infrared thermal imaging camera (T630sc, FLIR, USA).

EMI shielding measurements

EMI shielding measurements were conducted over the X-band frequency range of 8.2-12.4 GHz using a vector network analyzer (3672C, 10 MHz - 140 GHz, China Electronics Technology Group Corporation, China). The thickness of each sample was measured using a digital micrometer at three locations, including one central position and two positions near opposite edges. The standard deviation of the thickness measurements was 0.8 μm, suggesting limited thickness variation across the measured locations. The scattering parameters (S_{11} and S_{21}) were recorded, where S_{11} represents the reflection coefficient and S_{21} represents the transmission coefficient. The power coefficients of reflection (R), transmission (T), and absorption (A) were calculated as follows[8,19]:

$$R = |S_{11}|^2 \tag{2}$$

$$T = |S_{21}|^2 \tag{3}$$

$$A = 1 - R - T \tag{4}$$

The total EMI shielding effectiveness (SE_T), reflection shielding effectiveness (SE_R), and absorption shielding effectiveness (SE_A) were calculated using the following equations[19]:

$$SE_T = -10\log T = -10\log|S_{21}|^2 \tag{5}$$

$$SE_R = -10\log(1 - R) = -10\log(1 - |S_{11}|^2) \tag{6}$$

$$SE_A = SE_T - SE_R \tag{7}$$

$$SE/t = \frac{SE_T}{t} \tag{8}$$

RESULTS AND DISCUSSION

Fabrication and characterization of G@SiC NFFs

Constructing a ceramic-confined graphene fibrous architecture requires coordinated control over fiber formation, radial precursor distribution, and phase conversion[15,16,20]. As illustrated in Figure 1A and B, G@SiC NFFs were fabricated through sequential coaxial electrospinning, chemical reduction, oxidative curing, and thermal annealing[21]. During coaxial electrospinning, the GO/PAS core solution and PCS/PVP shell solution were spatially confined within the inner and outer channels, respectively, thereby defining the radial precursor arrangement[3,18]. Subsequent chemical and thermal conversion transformed this programmed architecture into a graphene fiber core encapsulated by a dense SiC ceramic shell while preserving the fibrous framework.

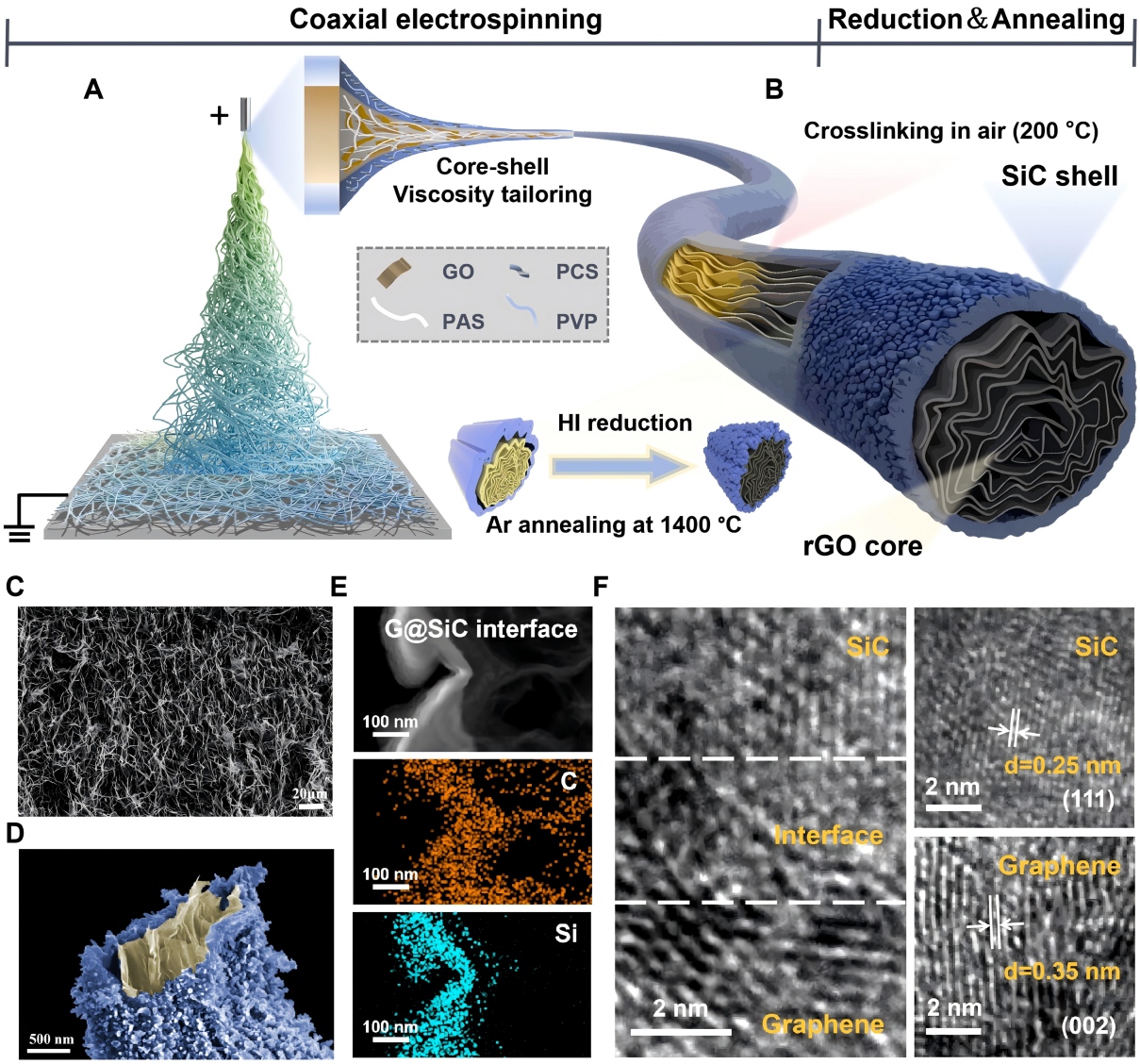


Figure 1. Fabrication and radial interfacial architecture of G@SiC NFFs. (A and B) Schematic illustration of the coaxial electrospinning and conversion route for constructing graphene-core/SiC-shell G@SiC NFFs; (C) SEM image of the as-prepared G@SiC NFF, showing a continuous interconnected nanofiber network; (D) Cross-sectional SEM image of an individual fiber with a distinct core-shell morphology. False colors are used for visual guidance; (E) TEM image and corresponding EDS elemental maps of C and Si, confirming a carbon-rich core and a Si-rich shell; (F) HRTEM image of the graphene fiber/SiC interfacial region, with enlarged regions showing lattice spacings of SiC (111) and graphitic carbon (002). G@SiC NFFs: Graphene@silicon carbide nanofiber fabrics; SEM: scanning electron microscopy; TEM: transmission electron microscopy; EDS: energy-dispersive X-ray spectroscopy; HRTEM: high-resolution transmission electron microscopy; GO: graphene oxide; PCS: polycarbosilane; PAS: polyacrylate; PVP: polyvinylpyrrolidone; rGO: reduced graphene oxide.

As shown in Figure 1C, the annealed fabric consists of abundant interconnected fibers, forming a continuous nonwoven network. The retention of the fibrous morphology after multistep conversion indicates that the electrospun framework remains structurally intact during chemical and thermal treatments[15]. Cross-sectional SEM observation of an individual fiber further reveals two regions with distinct contrast, where the outer region continuously encloses the inner domain [Figure 1D]. This contrast feature suggests that the coaxially electrospun core-shell architecture remains intact after multistep conversion.

TEM and elemental mapping reveal the nanoscale compositional distribution of the G@SiC nanofibers. As shown in Figure 1E, carbon is mainly concentrated in the inner region, whereas silicon is preferentially enriched near the periphery, confirming the formation of a carbon-rich core and a silicon-containing outer

shell. High-resolution TEM (HRTEM) imaging of the G@SiC interface resolves distinct lattice fringes from both domains [Figure 1F]. The shell region exhibits a lattice spacing of approximately 0.25 nm, characteristic of the SiC (111) plane, whereas the core region shows a spacing of approximately 0.35 nm, corresponding to the (002) plane of graphitic carbon[15,22,23]. These lattice features confirm the successful encapsulation of a graphitized carbon core within a dense SiC ceramic shell.

Rheological matching and chemical conversion of the core-shell precursor fibers

Stable coaxial electrospinning requires synchronized deformation of the core and shell jets during fluid delivery, compound Taylor cone formation, and subsequent electrohydrodynamic stretching[24]. As illustrated in Figure 2A, the outer shell fluid must confine the internal stream while maintaining sufficient deformability under the applied electric field. Insufficient shell viscosity weakens confinement of the core stream, causing incomplete encapsulation, non-uniform shell coverage, or partial core exposure. Conversely, excessive shell viscosity or viscoelastic mismatch suppresses jet elongation and destabilizes the compound jet, resulting in interrupted spinning, bead formation, or irregular fiber deposition. Because carbon filler spatial distribution governs conductive-network formation and electrical conductivity[25], continuous core-shell precursor fibers require not only intrinsically spinnable solutions but also rheological compatibility between the GO/PAS core and PCS/PVP shell solutions[26-29].

Rheological assessments and spinnability evaluations delineate the precise operational window required for stable coaxial fiber formation. The shear-rate-dependent viscosity curves reveal that all PCS/PVP shell solutions exhibit typical shear-thinning behavior [Figure 2B], which is favorable for electrospinning because it facilitates smooth fluid extrusion through the spinneret while preserving sufficient interchain cohesion before jet initiation. Furthermore, the viscosity varies markedly with the PVP concentration, confirming its critical role as a rheological modifier for the PCS precursor. A delicate rheological balance is therefore important. In this study, rheological compatibility was evaluated based on the combined consideration of the viscosity level within the processing-relevant shear-rate range, the shear-thinning response, and the frequency-dependent storage modulus (G'), loss modulus (G''), and loss tangent ($\tan\delta$). A favorable formulation was defined as one that balanced sufficient elasticity for core confinement with adequate fluidity for extrusion and electrohydrodynamic stretching. Inadequate shell viscosity failed to robustly encapsulate the core stream, whereas excessive viscosity severely impedes stretching and triggers unstable deposition. Consequently, the optimal shell formulation must precisely reconcile fluidic processability with the structural integrity necessary for continuous encapsulation.

Frequency-dependent storage and loss moduli provide deeper insights into the viscoelastic compatibility between the core and shell solutions [Figure 2C and Supplementary Figure 1]. Solution rheology is known to strongly influence electrospun jet stability and fiber formation[29]. Among the evaluated shell formulations, PVP6 demonstrates relatively stable moduli and optimal viscoelastic matching with the GO5 core, thereby ensuring synchronized deformation during coaxial jet formation and stretching. The loss tangent ($\tan\delta$) offers complementary perspectives on the dynamic balance between viscous dissipation and elastic recovery [Figure 2D]. A moderate and frequency-stable $\tan\delta$ is desirable because the shell fluid must effectively accommodate extensional stress while retaining adequate elasticity to preserve interfacial continuity. Subsequent extensional and spinnability evaluations further validate the rheological screenings [Figure 2E and Supplementary Figure 2]. Formulations lacking sufficient interchain entanglement undergo rapid capillary breakup during extension. Conversely, the optimized core-shell system sustains continuous and stable fluidic jets, manifesting superior resistance to capillary-driven droplet fragmentation.

Having established the optimal PVP content, we systematically investigated the interplay between the PCS concentration and the shell-to-core flow rate ratio. The spinnability map in Figure 2F summarizes the coefficient of variation of fiber diameter under different PCS concentrations and flow rate ratios, with the full

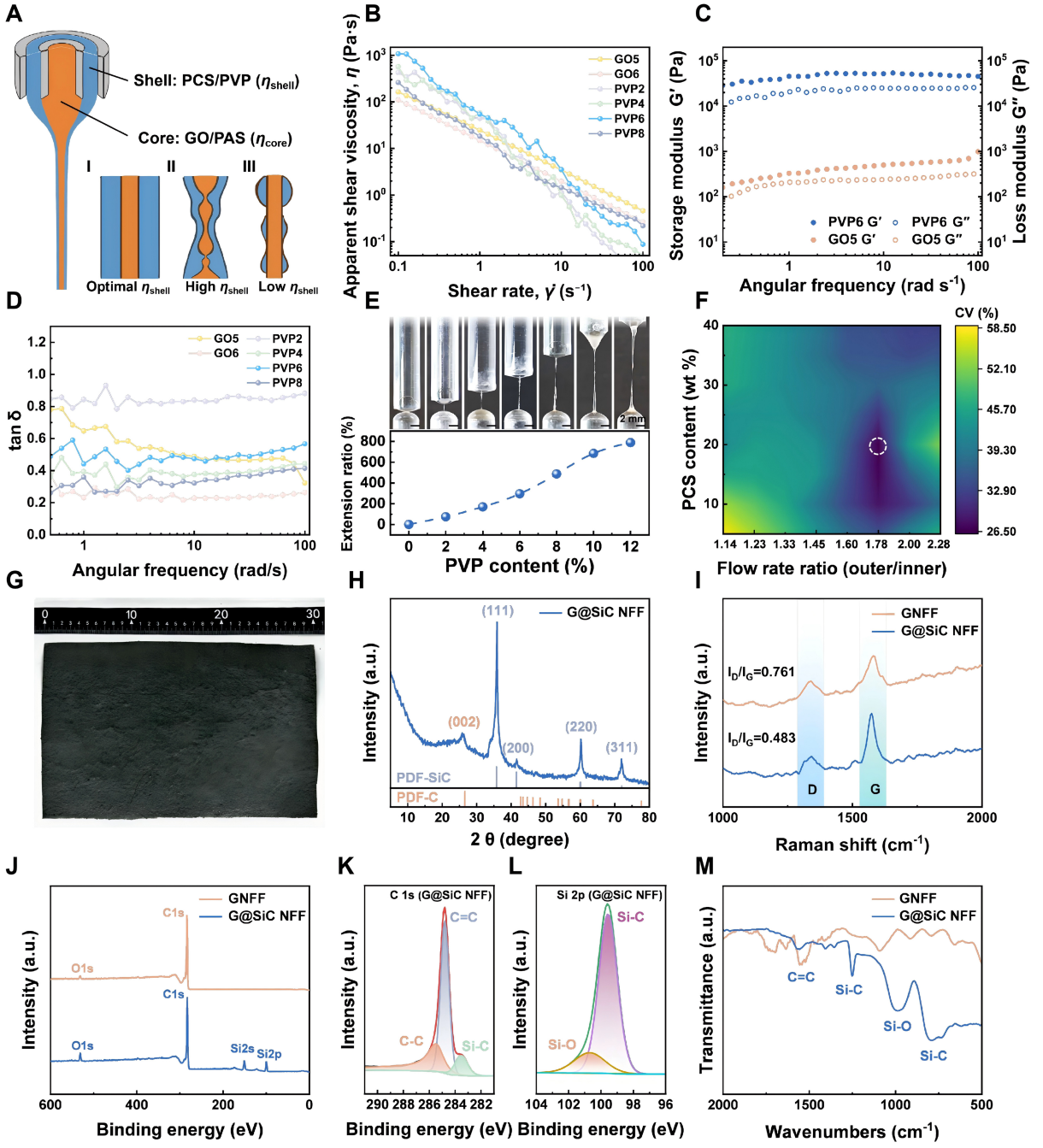


Figure 2. Rheological design and chemical evolution of G@SiC NFFs. (A) Schematic of coaxial flow configurations and jet states governed by core-shell rheological matching: I, stable core-shell jet; II, viscoelastic mismatch-induced jet instability; III, incomplete shell confinement with partial core exposure; (B) Shear-rate-dependent apparent viscosity of core and shell precursor solutions; (C) Frequency-dependent storage and loss moduli of representative precursor solutions; (D) Loss tangent (tanδ) of representative precursor solutions, indicating the viscoelastic balance; (E) Photographs and extension-ratio analysis showing the drawability of precursor solution; (F) Spinnability map as a function of PCS concentration and outer/inner flow-rate ratio. The white circle indicates the optimized spinning condition; (G) Photograph of a large-area freestanding G@SiC NFF; (H) XRD pattern of G@SiC NFF; (I) Raman spectra and (J) XPS survey of GNFF and G@SiC NFF; (K and L) High-resolution C 1s and Si 2p XPS spectra resolving C–C/C=C, C–O, Si–C, and Si-O bonding components; (M) FTIR spectra of GNFF and G@SiC NFF. G@SiC NFFs: Graphene@silicon carbide nanofiber fabrics; PCS: polycarbosilane; XRD: X-ray diffraction; XPS: X-ray photoelectron spectroscopy; GNFF: graphene nanofiber fabric; FTIR: Fourier-transform infrared spectroscopy; PVP: polyvinylpyrrolidone; GO: graphene oxide; PAS: polyacrylate.

diameter distributions shown in Supplementary Figure 3. During flow-rate optimization, the shell flow rate was maintained at 0.032 mL·min^{-1}, whereas the core flow rate was varied between 0.014 and 0.028 mL·min^{-1} to obtain shell-to-core flow-rate ratios of 1.14-2.28. Among all tested conditions, the combination of 20 wt%

PCS and a shell-to-core flow-rate ratio of 1.78 yielded the lowest coefficient of variation in fiber diameter, indicating a narrower diameter distribution. Consistently, SEM observations showed relatively uniform fibers, suggesting enhanced jet stability under these conditions. SEM characterization revealed that an insufficient PCS concentration (10 wt%) fails to supply adequate precursor for continuous shell encapsulation, while excessively high concentrations (30 and 40 wt%) led to structural artifacts, including severe fiber thickening, localized agglomeration, and bead defects [Supplementary Figure 4]. Accordingly, PVP6, a PCS concentration of 20 wt%, and a shell-to-core flow-rate ratio of 1.78 were selected as the baseline formulation and processing conditions for fabricating G@SiC precursor fibers. Samples with varied PCS and PVP contents were prepared according to the compositions specified for each comparison.

Under the optimized conditions, a large-area and freestanding fiber network with homogeneous fiber morphology was successfully realized. After sequential chemical reduction, oxidative curing, and high-temperature annealing, the color of the fabric changed from brownish yellow to brownish black, indicating the formation of a SiC shell [Figure 2G]. Cross-sectional SEM images revealed a continuous fibrous network and a relatively uniform SiC shell surrounding the individual G@SiC nanofibers [Supplementary Figure 5A and B]. The good flexibility of the G@SiC NFF is shown in Supplementary Figure 6. Tensile and cyclic deformation measurements further confirmed its mechanical flexibility [Supplementary Figure 7]. The tensile strain of the fabric could reach ~15%, while the resistance variation is highly recoverable during repeated stretching and bending cycles. Figure 2H shows the XRD pattern of the resultant fabric. A broad diffraction peak centered at ~26° is attributed to the (002) plane of graphitized carbon, whereas distinct diffraction peaks at 36.0°, 41.6°, 60.0°, and 72.0° can be assigned to crystalline SiC[21,23]. Comparative XRD patterns of G@SiC NFF, GNFF, and SiCNFF further support these phase assignments [Supplementary Figure 8]. Collectively, these results confirm the complete ceramization of the PCS-derived shell into a robust SiC phase during thermal conversion, as well as the formation of a graphene fiber core.

The characteristic D and G bands in the Raman spectra [Figure 2I] at approximately 1,350 and 1,580 cm^{-1} are assigned to defective carbon structures and the in-plane vibration of sp^2-bonded graphitic carbon, respectively[30]. Comparative Raman spectra of GNFF, GO@PCS, G@SiC NFF, SiC, and SiO_2 further clarify the carbon- and ceramic-related vibrational features [Supplementary Figure 9]. G@SiC NFF retains distinct D and G bands after the thermochemical conversion. Moreover, the I_D/I_G intensity ratio undergoes a sharp reduction from 0.761 in the pristine GNFF to 0.483 in G@SiC NFF. Since both samples were annealed at 1,400 °C, the lower I_D/I_G ratio of G@SiC NFF is unlikely to arise solely from the annealing temperature. It may instead be associated with the formation and reorganization of carbon-rich domains during PCS-to-SiC conversion and the development of the SiC/C interface[31]. Previous studies have reported the formation of graphitic carbon layers and interface-related structures on SiC surfaces, together with changes in their morphology and Raman response under different growth conditions[32]. These findings provide a relevant context for considering the role of SiC-C interfacial processes in the local carbon structure of G@SiC NFF. Because the Raman response is sensitive to near-surface and interfacial regions, the lower I_D/I_G ratio primarily indicates a difference in the local carbon structure probed by Raman spectroscopy.

The surface chemistry and bonding states were further investigated by XPS and FTIR analyses. The XPS survey spectra show that the pristine GNFF is mainly composed of C and O, whereas the G@SiC NFF exhibits a prominent Si signal alongside these elements [Figure 2J]. Given the inherent surface sensitivity of XPS, the pronounced Si signal in G@SiC NFF confirms the successful formation of the SiC shell. High-resolution deconvolution of the C 1s spectrum distinguishes specific bonding environments corresponding to Si–C, C–C/C=C, and C–O [Figure 2K][33]. The Si 2p spectrum resolves a dominant Si–C peak accompanied by a minor Si–O component [Figure 2L]. The synchronized emergence of Si–C features in both the C 1s and Si 2p spectra provides direct evidence of covalent silicon-carbon bonding, indicating that the PCS-derived

shell underwent ceramic conversion during thermal treatment. The minor Si–O contribution can be attributed to superficial oxidation or trace residual oxygen-containing species.

In the FTIR spectra displayed in Figure 2M, GNFF exhibits only weak infrared absorption, whereas G@SiC NFF shows distinct Si–C stretching vibrations accompanied by a weak Si–O band. Together with the XPS results, the FTIR spectra support the formation of Si–C bonds within the outer shell[10].

High-temperature oxidative stability of G@SiC NFFs

The oxidation resistance of G@SiC NFFs was first evaluated by TGA in an air atmosphere. As depicted in Figure 3A, the pristine GNFF undergoes rapid mass loss upon heating, reflecting oxidative ablation of the exposed carbon framework[5,6]. In contrast, the G@SiC NFF exhibits a drastically retarded degradation profile, retaining ~90.6% of its initial mass even at 650 °C. The PCS-concentration-dependent TGA curves further reveal the critical role of sufficient ceramic-shell formation in suppressing oxidative mass loss [Supplementary Figure 10]. The SiCNFF exhibits relatively high thermo-oxidative stability, with a slight mass loss at intermediate temperatures followed by a gradual mass gain above approximately 1,000 °C, consistent with the oxidation behavior of SiC and the formation of a nonvolatile SiO_2 layer[16,17]. This exceptional mass retention confirms that the SiC shell functions as an impenetrable physical barrier, effectively shielding the highly graphitized carbon core from direct oxygen attack[34]. Quantitative analysis of the initial mass loss and high-temperature mass gain further supports the oxidation-retarding effect of the SiC shell [Supplementary Figure 11]. The slight mass gain observed above approximately 1,000 °C is attributed to the passive oxidation of SiC and the formation of nonvolatile SiO_2 according to $SiC + 3/2O_2 \rightarrow SiO_2 + CO\uparrow$. The resulting SiO_2 layer impedes oxygen diffusion and retards further oxidation. In air, initial mass loss is markedly suppressed in the G@SiC NFF relative to bare GNFF and generally decreases with increasing PCS-derived SiC content. This protective encapsulation is also evidenced by the derivative thermogravimetric (DTG) profiles [Figure 3B]. Specifically, the temperature corresponding to the maximum degradation rate undergoes a remarkable shift from ~425 °C for the bare GNFF to ~685 °C for the G@SiC NFF. These results demonstrate that the core-shell encapsulation paradigm endows the conductive carbon network with unprecedented oxidative resilience in extreme, high-temperature environments.

This improved oxidative resistance guarantees stable electrical properties of the G@SiC NFFs under extreme conditions[1,35-37]. As shown in Figure 3C, during continuous exposure to an alcohol-lamp flame, pristine GNFF burns rapidly while the G@SiC NFF preserves its structural integrity with only moderate surface color change. Figure 3D and Supplementary Movie 1 demonstrate the normalized resistance evolution of both GNFF and G@SiC NFF during prolonged exposure to an alcohol-lamp flame at approximately 650 °C for 120 min. The GNFF rapidly loses electrical conductivity, which is a direct consequence of the oxidative ablation of its exposed carbon network. By contrast, the G@SiC NFF maintains stable resistance throughout the flame exposure, with the resistance fluctuation ($|\Delta R/R_0|$) remaining below 13%. This minimal deviation indicates that the conductive pathways within the graphene fiber core remain intact, shielded from the thermo-oxidative stress[36,38].

After annealing in ambient air at 650 °C for 1 h [Figure 3E], the unprotected GNFF was completely decomposed, while the G@SiC NFF remained an intact freestanding membrane. Under localized exposure to an alcohol-torch flame (~1,100 °C) for 180 s, G@SiC NFF retained its macroscopic integrity [Figure 3F]. SEM observations before and after the 180 s torch exposure further showed that the fibrous network morphology was largely preserved [Supplementary Figure 12]. In a separate time-dependent experiment, G@SiC NFF retained more than 87% of its initial mass after torch exposure for up to 200 s [Supplementary Figure 13].

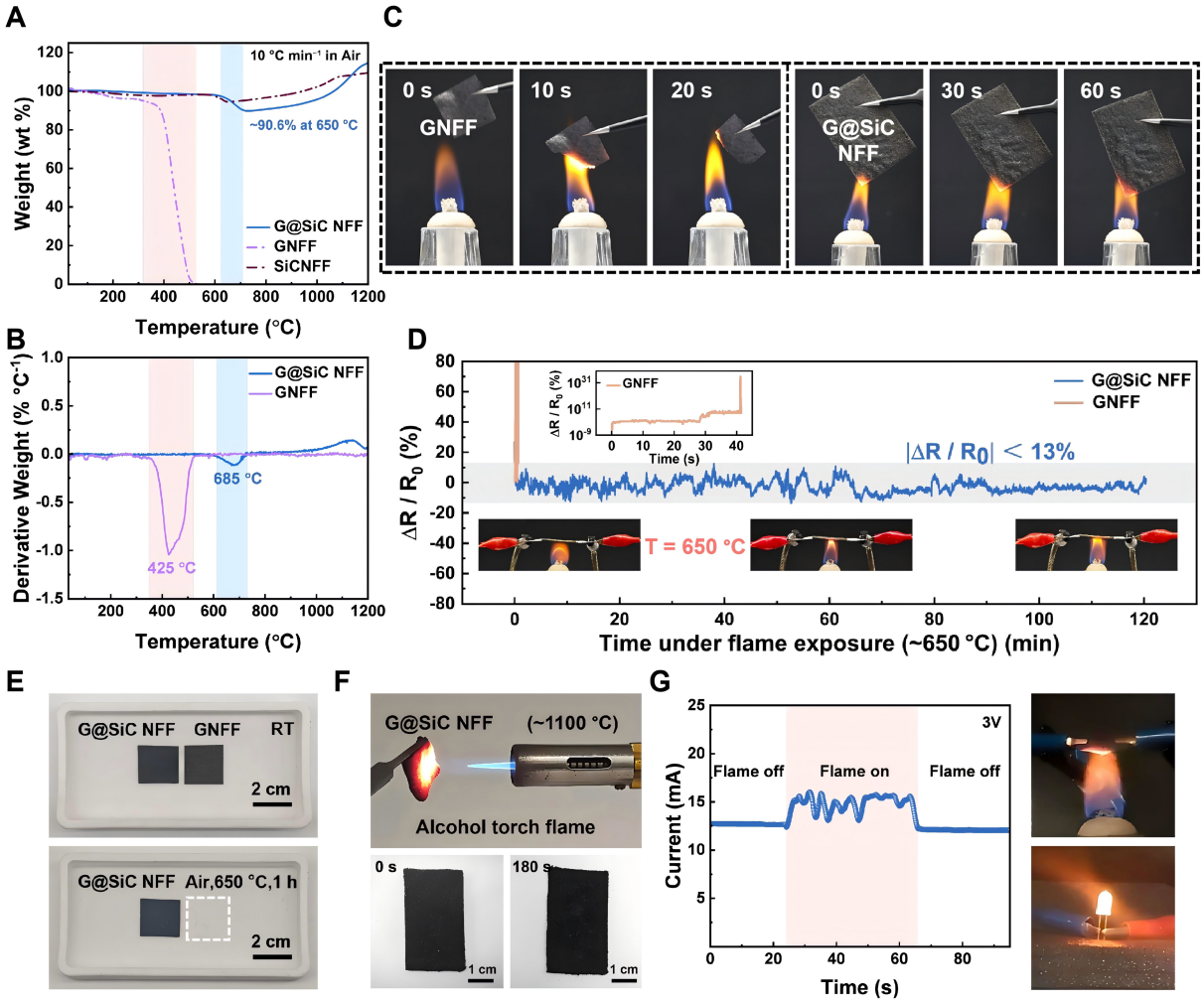


Figure 3. Thermo-oxidative stability and flame-tolerant electrical transport in G@SiC NFFs. (A) TGA profiles of GNFF, G@SiC NFF, and SiCNFF in an air atmosphere; (B) DTG profiles corresponding to (A); (C) Sequential photographs comparing the structural evolution of GNFF and G@SiC NFF under direct exposure to an alcohol-lamp flame; (D) Normalized resistance change of GNFF and G@SiC NFF during exposure to an alcohol-lamp flame (~650 °C); (E) Photographs of GNFF and G@SiC NFF before and after thermal annealing in air at 650 °C for 1 h; (F) Thermal shock testing of G@SiC NFF using an alcohol-torch flame (~1,100 °C) for 180 s; (G) Real-time current response and a series LED circuit utilizing G@SiC NFF as the conductive element, withstanding continuous exposure to an alcohol-lamp flame. All photographs in (C), (E), (F), and (G) were taken by the authors. G@SiC NFFs: Graphene@silicon carbide nanofiber fabrics; TGA: thermogravimetric analysis; GNFF: graphene nanofiber fabric; SiCNFF: silicon carbide nanofiber fabric; DTG: derivative thermogravimetric; LED: light-emitting diode; RT: room temperature.

To visually demonstrate this robust electrical continuity, the G@SiC NFF was integrated as the primary conductive interconnect in a series light-emitting diode (LED) circuit operating directly within the open flame [Figure 3G]. The sustained LED illumination confirms the uninterrupted charge-transport capability endowed by this core-shell architecture under extreme thermal conditions, as further visualized in Supplementary Movie 2. A separate 30 s flame-exposure demonstration is provided in Supplementary Movie 3.

Collectively, these results show that the dense SiC shell functions as a ceramic barrier that effectively shields the highly conductive graphene fiber core from severe oxidative degradation, preserving both the structural integrity and the interconnected charge-transport pathways under high-temperature oxidative conditions. These structural and electrical advantages provide a critical basis for durable EMI shielding performance under thermo-oxidative conditions[33].

EMI shielding in high-temperature oxidative environments

The EMI shielding performance of G@SiC NFF was evaluated across the X-band using scattering parameters obtained by vector network analysis. The total shielding effectiveness (SE_T), absorption contribution (SE_A), and reflection contribution (SE_R) were derived from the measured S-parameters based on the power-balance principle[8,19]. As summarized in Figure 4A, both electrical conductivity and post-oxidation residual mass depend on PCS content. Increasing the PCS loading increases the ceramic fraction and thereby improves thermo-oxidative mass retention. However, excessive PCS loading simultaneously reduces the bulk electrical conductivity because the SiC phase partially interrupts the conductive graphene nanofiber network. This trade-off decides the optimum design of the core-shell architecture: the SiC shell must provide sufficient conformal continuity to protect the graphene nanofiber core against oxidative ablation, while the internal conductive fiber network must retain electrical percolation to sustain charge transport and electromagnetic attenuation. Therefore, the ultimate EMI shielding response is determined not only by the content of the conductive phase, but also by the balance among electrical percolation, ceramic protection, and graphene/SiC interfacial polarization[39].

The EMI shielding performance of the selected G@SiC NFFs is shown in Figure 4B. All samples were tested at a fixed thickness of 40 μm. Under identical thickness conditions, all samples tested in Figure 4B exhibit SE_T values above 20 dB in the X-band, meeting the commonly accepted threshold for practical EMI shielding[40]. GPCS15 shows the highest SE_T of approximately 37 dB, suggesting an optimal balance among electrical conduction, impedance matching, and ceramic protection. Further increasing the PCS content improves ceramic coverage but disrupts charge transport through the graphene nanofiber network, leading to reduced shielding effectiveness. For all samples, SE_A is substantially higher than SE_R, indicating that electromagnetic waves are mainly dissipated within the hierarchical fibrous network rather than reflected at the surface. This absorption-dominated shielding behavior is desirable for mitigating secondary electromagnetic radiation[11,19].

The thickness-dependent EMI shielding performance is consistent with enhanced electromagnetic attenuation through extended internal propagation and dissipation pathways. As shown in Figure 4C, the frequency-averaged X-band SE_T of the G@SiC NFFs increases from approximately 12 dB at a thickness of 25 μm to over 80 dB at thicknesses of approximately 85-95 μm. At a nominal thickness of 85 μm, the G@SiC NFFs exhibit a frequency-averaged SE_T of 81.03 ± 5.14 dB (85.5 dB for a representative 80 μm-thick specimen). Meanwhile, the thickness-normalized shielding effectiveness reaches approximately 10^3 dB·mm^{-1}, despite a thickness below 0.1 mm. This value compares favorably with those reported for ultrathin flexible EMI shielding materials[41,42]. Notably, the increase in SE_T mainly originated from the enhanced SE_A, whereas SE_R remained nearly constant. Because reflection is primarily governed by the impedance mismatch at the air-material interface, the identical composition and comparable surface characteristics of the specimens resulted in only minor changes in SE_R with increasing thickness. In contrast, a greater thickness increased the effective propagation distance within the porous fibrous network, providing more opportunities for conductive loss, interfacial polarization, and internal scattering/multiple reflections at the fiber surfaces, pore interfaces, and G@SiC core-shell interfaces[9]. Thus, the thickness-dependent enhancement in SE_T was predominantly absorption-driven. The EMI shielding retention characteristics of 80 μm-thick G@SiC NFFs prepared using a precursor formulation containing 20 wt% PCS were subsequently investigated after prolonged thermo-oxidative exposure. Figure 4D shows the frequency-dependent SE_T before and after isothermal oxidation in ambient air at elevated temperatures. After high-temperature treatment at 400 °C for 1 h, SE_T of the SiC-protected fabric decreases slightly and remains close to 80 dB across the measured frequency range. Even after oxidation at 650 °C for 1 h, the average SE_T remains above 76.7 dB. The temperature-dependent summary in Figure 4E further confirms that the SE_T shows strong resistance to oxidative degradation, with absorption (SE_A) governing the overall attenuation across the X-band [Figure 4F]. Frequency-resolved decomposition of SE_T after 650 °C oxidation further supports this absorption-

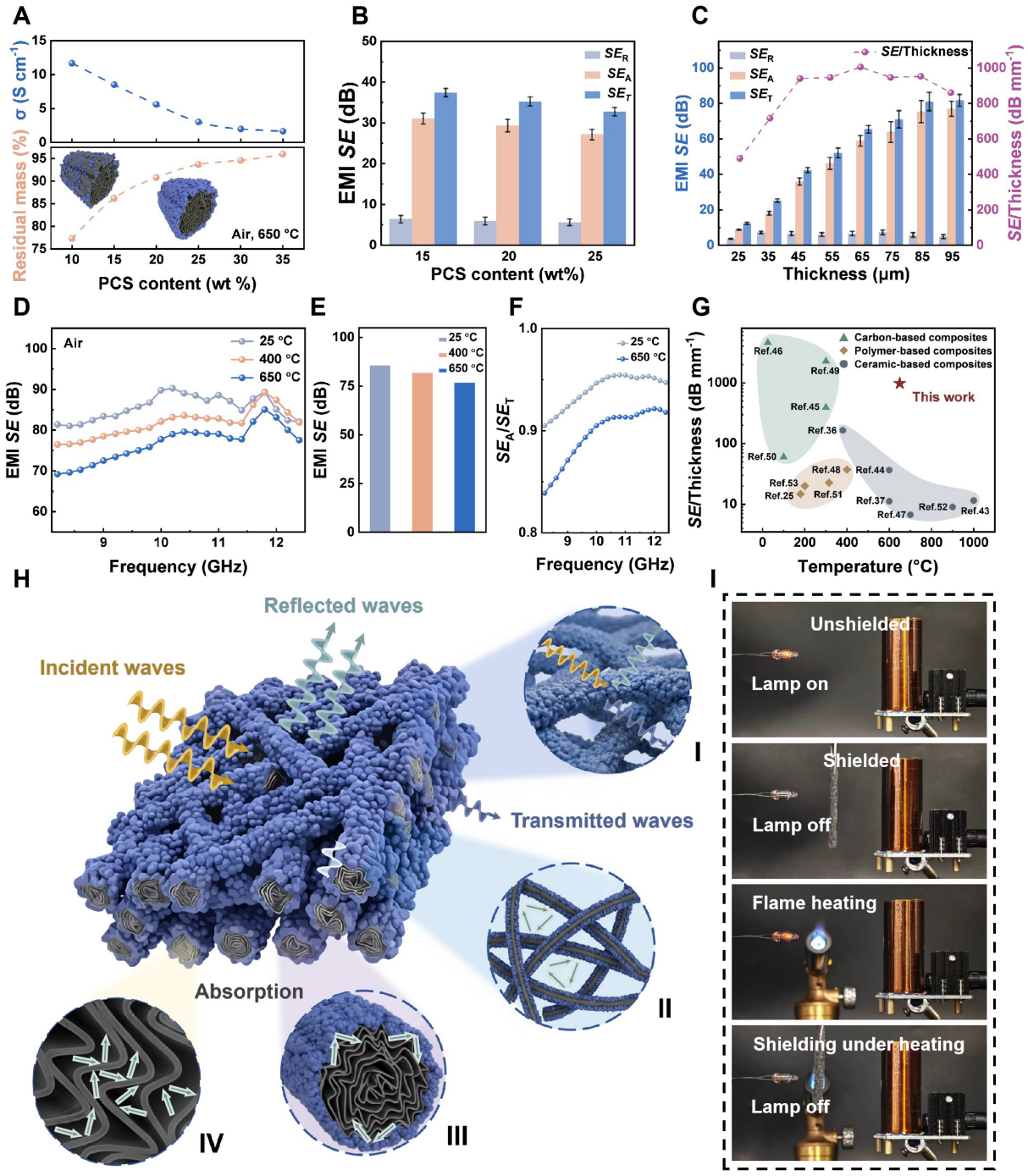


Figure 4. EMI shielding retention of G@SiC NFF after oxidative heating. (A) Electrical conductivity and residual mass of G@SiC NFFs as a function of PCS content after oxidation in air at 650 °C; (B) X-band total shielding effectiveness, absorption contribution, and reflection contribution of G@SiC NFFs derived from precursor formulations with different PCS contents, measured at a fixed thickness of 40 μm; (C) Thickness-dependent shielding effectiveness and thickness-normalized shielding effectiveness of G@SiC NFF; (D) Frequency-dependent SE_T before and after oxidative heating at 400 and 650 °C; (E) Average SE_T after oxidative heating at different temperatures; (F) Frequency-dependent SE_A/SE_T ratio showing the retained absorption-dominated shielding mode before and after oxidative heating; (G) Comparison of G@SiC NFF with representative high-temperature EMI shielding materials; (H) Schematic illustration of the EMI shielding mechanism in the hierarchical G@SiC NFF; (I) Visual demonstration of shielding stability under exposure to an alcohol-torch flame at approximately 1,100 °C. Error bars in (B) and (C) represent SD from three independently measured 5 cm × 5 cm films for electromagnetic shielding measurements. All photographs in (I) were taken by the authors. EMI: Electromagnetic interference; G@SiC NFF: graphene@silicon carbide nanofiber fabric; PCS: polycarbosilane; SD: standard deviation.

dominated shielding mechanism across the X-band [Supplementary Figure 14]. The high-temperature EMI shielding performance of G@SiC NFF was further benchmarked against representative EMI shielding materials designed for high-temperature environments [Figure 4G][25,36,37,43-53]. Detailed comparison data are provided in Supplementary Table 1. Compared with previously reported metal-based, carbon-based, polymer-based, and ceramic-containing shields, G@SiC NFF combines high shielding effectiveness, small thickness, and oxidation tolerance, exhibiting excellent comprehensive performance.

This advantage stems from the hierarchical G@SiC core-shell architecture. As schematically illustrated in Figure 4H, a small portion of incident electromagnetic waves is initially reflected when encountering the fabric because of the impedance mismatch between air and the conductive network (I). The primary attenuation occurs after the electromagnetic waves penetrate the porous three-dimensional network. The interconnected nanofibers induce multiple internal reflections and scattering, thereby extending the propagation pathways of the incident waves (II). The SiC shell and G@SiC heterointerfaces may contribute to dielectric relaxation and interfacial polarization under the alternating electromagnetic field, as reported for related carbon/SiC and carbon-based heterostructures[23,33,54,55] (III). Meanwhile, the wrinkled rGO core provides a conductive scaffold that facilitates carrier migration and ohmic dissipation[1,2] (IV). Furthermore, the surface roughness of the ceramic shell increases local field heterogeneity and expands the effective interfacial area, promoting additional scattering and polarization relaxation. The synergy of these coupled electromagnetic processes accounts for the absorption-dominated EMI shielding behavior and its retention after thermal oxidation. The practical shielding durability of the G@SiC NFF was qualitatively demonstrated under direct exposure to an alcohol-torch flame with a nominal temperature of approximately 1,100 °C [Figure 4I]. When the G@SiC NFF was placed between the electromagnetic source and the indicator lamp, the lamp remained off during flame exposure, indicating that the film retained its electromagnetic-shielding function under flame-induced thermal shock.

Robust Joule heating functionality in oxidative atmospheres

Beyond serving as a robust thin film for passive electromagnetic protection, the preserved electrical networks and outstanding thermo-oxidative resilience of the G@SiC NFFs suggest their potential for active electrothermal heating in oxidative atmospheres, where carbon-based conductive networks commonly suffer from rapid oxidation and electrical failure at elevated temperatures.

The electrothermal behavior of core-shell G@SiC NFF was first investigated under different driving voltages[56]. As shown in Figure 5A, the G@SiC NFF exhibits a rapid and reversible Joule heating response under applied voltages from 5 to 35 V. Upon electrical bias, the surface temperature increases rapidly and reaches a stable plateau within 0.14-0.35 s. Once the voltage is switched off, the fabric rapidly cools back to the ambient state. Detailed transient heating-rate profiles and enlarged cooling curves further confirm the rapid thermal activation and efficient heat dissipation of the G@SiC NFF across the examined voltage range [Supplementary Figure 15]. The steady-state temperature can be continuously regulated by the applied voltage, increasing from 52.4 °C at 5 V to 651.7 °C at 35 V. Furthermore, the approximately linear relationships between heating rate and power density and between steady-state temperature and U^2 confirm the Joule-heating-dominated electrothermal behavior of the G@SiC NFF [Supplementary Figure 16]. This broad voltage-programmable temperature window demonstrates that the G@SiC NFF can deliver tunable thermal outputs, spanning mild heating to high-temperature operation.

Infrared thermal images further reveal the spatial uniformity of Joule heating. As shown in Figure 5B, the fabric displays a homogeneous thermal distribution across all examined bias voltages, indicating a uniform conductive network and stable heat generation. The thermal response kinetics were further quantified in Figure 5C. Both the heating and cooling response times were in the sub-second regime, with t_{90} values of

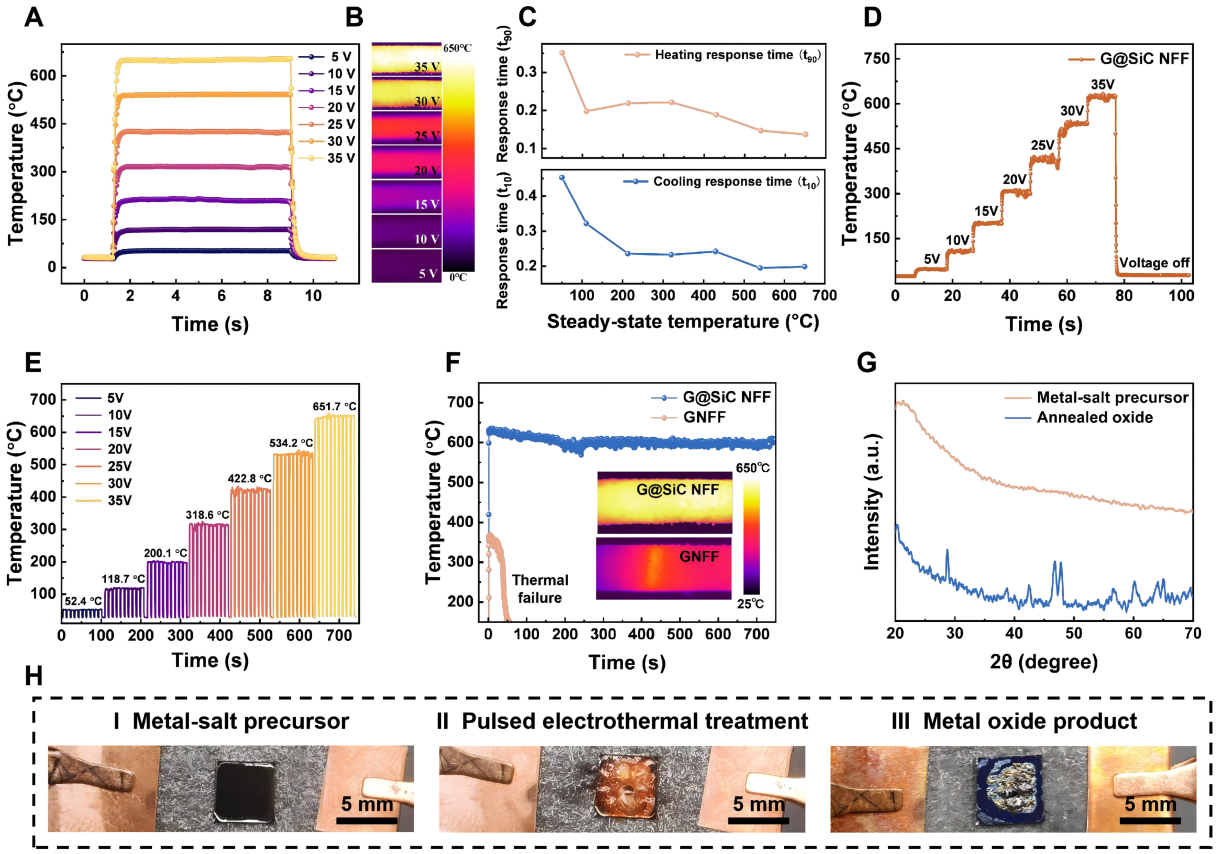


Figure 5. Rapid, stable, and high-temperature electrothermal functionality of G@SiC NFF in an air environment. (A) Time-dependent surface temperature of G@SiC NFF under different applied voltages, showing rapid voltage-programmable Joule heating and fast cooling; (B) Infrared thermal images of G@SiC NFF during Joule heating at different voltages; (C) Heating and cooling response times as a function of steady-state temperature; (D) Stepwise electrothermal response under programmed voltage loading; (E) Cyclic heating and cooling behaviour under repeated electrical stimulation at different voltages; (F) Long-term high-temperature Joule-heating stability of G@SiC NFF at approximately 600 °C compared with pristine GNFF; (G) XRD patterns of the metal-salt precursor and the electrothermally annealed oxide; (H) Optical photographs showing ultrafast electrothermal conversion of metal-salt precursors into metal oxides using G@SiC NFF as a localized high-temperature heating platform. All photographs in (H) were taken by the authors. G@SiC NFF: Graphene@silicon carbide nanofiber fabric; GNFF: graphene nanofiber fabric; XRD: X-ray diffraction.

0.14-0.35 s and t_{10} values of 0.19-0.45 s, respectively. Because these measurements were conducted under different applied voltages, the shorter t_{90} at higher steady-state temperatures reflects the greater Joule-heating power, whereas the shorter t_{10} at higher initial temperatures is attributed to enhanced heat dissipation, particularly thermal radiation. Under stepwise voltage loading, the surface temperature follows the applied voltage in a clear stepwise manner and stabilizes at each thermal plateau [Figure 5D], verifying voltage-dependent thermal regulation. During cyclic on/off tests under repeated electrical stimulation, the fabric exhibits highly reproducible heating and cooling profiles at different voltages [Figure 5E]. No obvious temperature decay, response delay, or unstable fluctuation is observed during repeated stimulation, demonstrating the good reversibility and short-cycle electrothermal stability.

The protective role of the SiC shell becomes particularly important during long-term high-temperature Joule heating in air. As shown in Figure 5F, pristine GNFF can initially be electrically heated to 350 °C for a short period; however, its surface temperature rapidly decreases after sudden electrical failure. This degradation is attributed to severe thermo-oxidative erosion of the exposed carbon network during high-temperature operation in ambient air. In contrast, the G@SiC NFF maintains stable Joule heating at approximately 600 °C over a prolonged duration, with minor temperature fluctuations. This comparison confirms that the SiC shell

effectively suppresses oxidative damage to the encapsulated conductive framework, thereby preserving electrical continuity and sustained heat output under harsh oxidative conditions[15,17,36].

Taking advantage of its favorable electrothermal properties, the G@SiC NFF was employed as a localized heating platform for the rapid conversion of an In/Ga/Zn-containing metal-salt precursor. This pulse-assisted electrothermal conversion is conceptually related to pulse Joule-heating synthesis, in which transient high temperatures enable rapid material transformation[57]. The G@SiC NFF used for the electrothermal treatment had dimensions of approximately 2.0 cm × 1.5 cm × 1.0 mm (length × width × apparent thickness). The precursor was subjected to ten electrothermal pulses, each consisting of 30 s of heating followed by a 10 s interval. As shown in Figure 5G, the untreated precursor exhibits a broad amorphous-like diffraction background, whereas the electrothermally treated product displays several weak diffraction features, indicating structural evolution and increased ordering during electrothermal treatment. Given the compositional and structural complexity of In-Ga-Zn-O materials, these diffraction features are not assigned to specific crystalline phases. Semi-quantitative SEM-EDS analysis further detected In, Ga, Zn, and O in the treated product [Supplementary Figure 17 and Supplementary Table 2]. Collectively, these results are consistent with the rapid formation of an In-Ga-Zn-O multicomponent oxide product through pulse-assisted electrothermal conversion. The optical photographs in Figure 5H further show the visible color change of the precursor droplets after treatment, consistent with the electrothermal conversion of metal-salt precursors into oxide products. This proof-of-concept demonstration highlights the capability of G@SiC NFF to generate a localized high-temperature field under oxygen-containing conditions, offering a rapid route for oxide synthesis.

CONCLUSION

In summary, we demonstrate a graphene-core/SiC-shell nanofiber architecture for constructing flexible G@SiC NFFs that integrate electrical conductivity with thermo-oxidative stability, enabling durable EMI shielding and active electrothermal heating in ambient air. In this core-shell architecture, the interconnected graphene nanofiber core maintains continuous electron transport, while the SiC ceramic shell provides an oxidation-resistant external interface. A representative 20 wt% PCS-derived G@SiC NFF (~80 μm) exhibited an X-band EMI shielding effectiveness of 85.5 dB before oxidation and 76.7 dB after oxidation in air at 650 °C for 1 h, retaining 89.7% of its initial performance. The hybrid fabric also maintained stable electrothermal performance during prolonged exposure to an alcohol-lamp flame at 650 °C and thermal shock using an alcohol-torch flame at 1,100 °C, while enabling voltage-tunable heating up to 650 °C in air. These results demonstrate that the graphene/ceramic NFF can reconcile electrical conductivity, electromagnetic attenuation, flexibility, and thermal durability within a fibrous platform, offering a versatile route toward high-temperature flexible electronics, aerospace electromagnetic protection, and multifunctional thermal-management fabrics.

DECLARATIONS

Authors' contributions

Writing - original draft, validation, methodology, investigation, formal analysis: Lu, S.
Validation, supervision, investigation: Han, Z.
Validation, methodology, investigation: Shu, C.; Zheng, Z.
Validation, investigation: Zhou, Z.; Yao, Y.
Writing - review and editing, supervision, conceptualization: Han, Y.
Writing - review and editing, supervision, project administration, funding acquisition, conceptualization: Li, Z.; Jin, X.

Availability of data and materials

The authors declare that the primary data supporting the findings of this study are available within the paper and its Supplementary Materials. Additional data are available from the corresponding authors upon reasonable request.

AI and AI-assisted tools statement

An artificial intelligence tool, ChatGPT (version 5.5, released on 2026-04-23; OpenAI), was used during the preparation of this manuscript solely for language editing. This tool did not influence the study design, data collection, analysis, interpretation, or scientific content of the work. All authors take full responsibility for the accuracy, completeness, and final content of the manuscript.

Financial support and sponsorship

This work was financially supported by the Zhejiang Provincial Natural Science Foundation of China (LR25E020001), the National Natural Science Foundation of China (No. 52372051), and the Young Talents of Basic Research in Universities of Heilongjiang Province (YQJH2024073).

Conflicts of interest

Han, Y. is affiliated with Hangzhou Gaoxi Technology Co., Ltd., while the other authors declare no conflicts of interest.

Ethical approval and consent to participate

Not applicable.

Consent for publication

Not applicable.

Copyright

© The Author(s) 2026.

Supplementary Materials

Supplementary Materials

REFERENCES

1. Pang, K.; Liu, X.; Liu, Y.; et al. Highly conductive graphene film with high-temperature stability for electromagnetic interference shielding. *Carbon* **2021**, *179*, 202-8. DOI
2. Li, Z.; Xu, Z.; Liu, Y.; Wang, R.; Gao, C. Multifunctional non-woven fabrics of interfused graphene fibres. *Nat. Commun.* **2016**, *7*, 13684. DOI PubMed PMC
3. Han, Z.; Wang, J.; Liu, S.; et al. Electrospinning of neat graphene nanofibers. *Adv. Fiber. Mater.* **2022**, *4*, 268-79. DOI
4. Shu, C.; Han, Z.; Zheng, Z.; et al. Lightweight graphene-copper core-shell nanofiber fabric for highly efficient electromagnetic interference shielding. *Carbon* **2026**, *247*, 121061. DOI
5. Cho, J. Y.; Kim, J. H.; Han, J. T. Extraordinary thermal behavior of graphene oxide in air for electrode applications. *Nanoscale. Adv.* **2021**, *3*, 1597-602. DOI PubMed PMC
6. Hu, L.; Wang, A.; Wang, W. Structural evolution of graphene oxide and its thermal stability during high temperature sintering. *J. Wuhan. Univ. Technol. Mat. Sci. Edit.* **2022**, *37*, 342-9. DOI
7. Zhu, W.; Chen, Z.; Liang, J.; Su, D. A laminated carbon nanotubes/silicon boron carbonitride film for high-efficiency electromagnetic interference shielding with oxidation resistance. *Carbon* **2022**, *197*, 65-75. DOI
8. Nguyen, N. K.; Kim, D.; Phan, V. Q.; Kim, M.; Park, P.; Nah, J. Perspectives on absorption-dominant electromagnetic interference shielding materials with MXene and carbon-based polymer composites. *Carbon* **2025**, *238*, 120276. DOI
9. Zheng, S.; Wang, Y.; Wang, X.; Lu, H. Research progress on high-performance electromagnetic interference shielding materials with well-organized multilayered structures. *Mater. Today. Phys.* **2024**, *40*, 101330. DOI
10. Mei, H.; Zhao, X.; Gui, X.; et al. SiC encapsulated Fe@CNT ultra-high absorptive shielding material for high temperature resistant EMI shielding. *Ceram. Int.* **2019**, *45*, 17144-51. DOI
11. Park, B.; Hwang, S.; Lee, H.; et al. Absorption-dominant electromagnetic interference (EMI) shielding across multiple mmwave bands using conductive patterned magnetic composite and double-walled carbon nanotube film. *Adv. Funct. Mater.* **2024**, *34*, 2406197. DOI
12. Sun, R.; Lv, H.; Lian, G.; et al. Dielectric shell regulation in synergy FeCoNi@$ZnIn_2S_4$ microspheres with broadband electromagnetic wave absorption. *Soft. Sci.* **2025**, *5*, 35. DOI

13. Feng, Y.; Zhao, J.; Chen, K.; et al. CuS-bridged MXene-based photoresponsive phase change materials enabling thermoelectric cogeneration and microwave absorption. *Nanomicro. Lett.* **2026**, *18*, 428. DOI PubMed PMC
14. Yang, T.; Shen, Y.; Zhao, Z.; et al. Bioinspired multifunctional flexible C-SiC fibrous aerogel for superior electromagnetic interference shielding under extreme environments. *Adv. Sci.* **2026**, *13*, e76343. DOI PubMed PMC
15. Kang, W.; Shen, Y.; Yang, T.; Zhao, Z.; Gou, Y. Multifunctional submicron SiC fibers for extreme environments: superior electromagnetic absorption and high-temperature performance. *Adv. Funct. Mater.* **2025**, *35*, 2415432. DOI
16. Zhao, Z.; Liao, W.; Chen, J.; Jiao, J.; Wu, C.; Gou, Y. Advanced research on the preparation and application of carbide ceramic fibers. *J. Adv. Ceram.* **2024**, *13*, 1291-336. DOI
17. Li, Z.; Zhang, X.; Zhang, Q.; Avcu, E.; Withers, P. J.; Xiao, P. Oxidation and mechanical properties of SiC fibers after high temperature exposure in air and steam. *J. Eur. Ceram. Soc.* **2024**, *44*, 6864-74. DOI
18. Li, Y.; Wang, Y.; Li, Z.; et al. Meter-scale wearable multifunctional core-shell nanofiber textiles for ultra-broadband electromagnetic interference shielding and infrared stealth. *Adv. Mater.* **2025**, *37*, e2501485. DOI PubMed
19. Zhang, S.; Zhang, S.; Zhu, P.; et al. Recent achievements and performance of nanomaterials in microwave absorption and electromagnetic shielding. *Adv. Colloid. Interface. Sci.* **2025**, *335*, 103336. DOI PubMed
20. Huang, Y.; Wan, C. Controllable fabrication and multifunctional applications of graphene/ceramic composites. *J. Adv. Ceram.* **2020**, *9*, 271-91. DOI
21. Wang, B.; Wang, Y.; Lei, Y.; Wu, N.; Gou, Y.; Han, C. Tailoring of porous structure in macro-meso-microporous SiC ultrathin fibers *via* electrospinning combined with polymer-derived ceramics route. *Mater. Manuf. Process.* **2016**, *31*, 1357-65. DOI
22. Román-Manso, B.; Figueiredo, F. M.; Achiaga, B.; et al. Electrically functional 3D-architectured graphene/SiC composites. *Carbon* **2016**, *100*, 318-28. DOI
23. Chen, Y.; Peng, H.; Cai, B.; et al. Synthesis of ultralight hollow SiC/C nanofiber for highly efficient electromagnetic wave absorption. *J. Adv. Ceram.* **2026**, *15*, 9221225. DOI
24. Sun, Z.; Zussman, E.; Yarin, A.; Wendorff, J.; Greiner, A. Compound core–shell polymer nanofibers by co-electrospinning. *Adv. Mater.* **2003**, *15*, 1929-32. DOI
25. Liu, T.; Zhou, R.; Fei, Y.; et al. Spatially directed carbon nanotube enrichment via polylactide stereocomplex formation enables exceptional thermal stability, high thermal conductivity, and electromagnetic interference shielding. *Compos. Commun.* **2025**, *60*, 102627. DOI
26. Lin, J.; Yu, J.; Chen, F.; et al. A high-performance flexible coaxial BTO/PAN piezoelectric nanofibers for facial expression analysis. *Chem. Eng. J.* **2025**, *516*, 163932. DOI
27. Jia, X.; He, K.; Cai, L.; et al. Coaxially fabricated electrospinning near-infrared light-responsive nanofibrous membranes for combating drug-resistant bacteria. *J. Hazard. Mater.* **2025**, *492*, 138106. DOI PubMed
28. Cho, Y.; Beak, J. W.; Sagong, M.; Ahn, S.; Nam, J. S.; Kim, I. D. Electrospinning and nanofiber technology: fundamentals, innovations, and applications. *Adv. Mater.* **2025**, *37*, e2500162. DOI PubMed PMC
29. Dong, S.; Maciejewska, B. M.; Schofield, R. M.; Hawkins, N.; Siviour, C. R.; Grobert, N. Electrospinning nonspinnable sols to ceramic fibers and springs. *ACS. Nano.* **2024**, *18*, 13538-50. DOI PubMed PMC
30. Lipatov, A.; Guinel, M. J.; Muratov, D. S.; et al. Low-temperature thermal reduction of graphene oxide: *in situ* correlative structural, thermal desorption, and electrical transport measurements. *Appl. Phys. Lett.* **2018**, *112*, 053103. DOI
31. Colombo, P.; Mera, G.; Riedel, R.; Sorarù, G. D. Polymer-derived ceramics: 40 years of research and innovation in advanced ceramics. *J. Am. Ceram. Soc.* **2010**, *93*, 1805-37. DOI
32. Emtsev, K. V.; Bostwick, A.; Horn, K.; et al. Towards wafer-size graphene layers by atmospheric pressure graphitization of silicon carbide. *Nat. Mater.* **2009**, *8*, 203-7. DOI
33. Li, Z.; Wang, Y. Preparation of polymer-derived graphene-like carbon-silicon carbide nanocomposites as electromagnetic interference shielding material for high temperature applications. *J. Alloys. Compd.* **2017**, *709*, 313-21. DOI
34. Ren, X.; Li, H.; Fu, Q.; Li, K. $Ta_xHf_{1-x}B_2$–SiC multiphase oxidation protective coating for SiC-coated carbon/carbon composites. *Corros. Sci.* **2014**, *87*, 479-88. DOI
35. Zhang, Q.; Lin, D.; Deng, B.; et al. Flyweight, superelastic, electrically conductive, and flame-retardant 3D multi-nanolayer graphene/ceramic metamaterial. *Adv. Mater.* **2017**, *29*, 1605506. DOI PubMed
36. Wang, C.; Xu, Q.; Hu, J.; et al. Graphene/SiC-coated textiles with excellent electromagnetic interference shielding, Joule heating, high-temperature resistance, and pressure-sensing performances. *J. Adv. Ceram.* **2023**, *12*, 778-91. DOI
37. Hou, Y.; Cheng, L.; Zhang, Y.; Du, X.; Zhao, Y.; Yang, Z. High temperature electromagnetic interference shielding of lightweight and flexible ZrC/SiC nanofiber mats. *Chem. Eng. J.* **2021**, *404*, 126521. DOI
38. Yin, C.; Li, X.; Chen, P.; Kale, G. M.; Zhu, B. Oxidation resistance and wettability of graphite/SiC composite. *IJMR* **2018**, *109*, 629-37. DOI

39. Mu, Y.; Zhou, W.; Wan, F.; Ding, D.; Hu, Y.; Luo, F. High-temperature dielectric and electromagnetic interference shielding properties of SiCf/SiC composites using Ti_3SiC_2 as inert filler. *Compos. Part. A. Appl. Sci. Manuf.* **2015**, *77*, 195-203. DOI
40. Cheng, J.; Li, C.; Xiong, Y.; et al. Recent advances in design strategies and multifunctionality of flexible electromagnetic interference shielding materials. *Nanomicro. Lett.* **2022**, *14*, 80. DOI PubMed PMC
41. Xie, F.; Liu, Q.; Dai, X.; Wei, H.; Lu, Z. Highly durable hollow sandwich MXene/h-AgNWs/ANF composite films for exceptional electromagnetic interference shielding performance. *Compos. Sci. Technol.* **2024**, *256*, 110766. DOI
42. Lai, D.; Chen, X.; Xu, X.; Wang, G.; Wang, Y. Elastomeric foldable and high-temperature endurance porous graphene films with superior electromagnetic interference shielding performance. *Ind. Eng. Chem. Res.* **2022**, *61*, 1122-32. DOI
43. Li, Y.; Deng, C.; Zhao, Z.; Han, L.; Lu, P.; Wang, Y. Carbon fiber-based polymer composite via ceramization toward excellent electromagnetic interference shielding performance and high temperature resistance. *Compos. Part. A. Appl. Sci. Manuf.* **2020**, *131*, 105769. DOI
44. Qing, Y.; Yao, H.; Li, Y.; Luo, F. Plasma-sprayed ZrB_2/Al_2O_3 ceramics with excellent high temperature electromagnetic interference shielding properties. *J. Eur. Ceram. Soc.* **2021**, *41*, 1071-5. DOI
45. Liu, L. X.; Chen, W.; Zhang, H. B.; et al. Super-tough and environmentally stable aramid. nanofiber@MXene coaxial fibers with outstanding electromagnetic interference shielding efficiency. *Nanomicro. Lett.* **2022**, *14*, 111. DOI PubMed PMC
46. Da, Y.; Qu, Q.; Kong, L.; et al. A high-performance, oxidation resistance and flexible Zn@MXene/cellulose nanofibers electromagnetic shielding film. *RSC. Adv.* **2023**, *13*, 6619-29. DOI PubMed PMC
47. Yang, F.; Yao, J.; Du, W.; et al. Ice-templated assembly strategy to construct oriented porous Ti_3SiC_2 ceramics for thermal management and electromagnetic interference shielding in harsh thermal environments. *J. Eur. Ceram. Soc.* **2023**, *43*, 3112-21. DOI
48. Mei, X.; Wu, T.; Liang, L.; et al. Poly aryletherketone chemically modified multi-walled carbon nanotubes/poly etheretherketone electromagnetic interference shielding foam suitable for high temperature and strong corrosive media. *Mater. Today. Nano.* **2024**, *28*, 100538. DOI
49. Shen, Y.; Yue, Y.; Li, H.; et al. Robust alternating multilayered MXene/CNT films for high-performance EMI shielding and Joule heating with superior fire/oxidation resistance. *Sci. China. Mater.* **2025**, *68*, 4144-54. DOI
50. Si, Z.; Yan, Y.; Liu, X.; et al. Flexible and multifunctional microcrystalline cellulose/$Ti_3C_2T_x$ MXene-POSS composite films for electromagnetic interference shielding in extreme environments. *Chem. Eng. J.* **2025**, *525*, 169897. DOI
51. Wang, N.; Li, X.; Cao, W.; et al. Lightweight polyimide nanocomposites with 3D cocarbonized MXene/carbon fiber networks for electromagnetic interference shielding and high-temperature stability. *ACS. Appl. Nano. Mater.* **2025**, *8*, 7347-59. DOI
52. Zhu, W.; Xia, X.; Zheng, Y.; Ji, H.; Su, D. Tailoring of carbon structure in lightweight GNS/SiBCN nanocomposites for enhanced electromagnetic interference shielding performance. *J. Eur. Ceram. Soc.* **2025**, *45*, 117180. DOI
53. Liu, S.; Zhan, Y.; Sun, J.; et al. High-temperature stable liquid crystalline polymer/carbon nanotube composites with a “brick-mortar” segregated structure for electromagnetic interference shielding. *Compos. Commun.* **2026**, *62*, 102720. DOI
54. Chen, J.; Du, Y.; Wang, Z.; et al. Anchoring of SiC whiskers on the hollow carbon microspheres inducing interfacial polarization to promote electromagnetic wave attenuation capability. *Carbon* **2021**, *175*, 11-9. DOI
55. Guo, S.; Zhang, J.; Lin, C.; Ge, J.; Bi, S.; Hou, Z. L. Multilayer core–shell structured $FeNi_3$@C with enhanced interfacial polarization for microwave absorbers. *Nano. Res.* **2025**, *18*, 94907151. DOI
56. Feng, Z.; Ye, H.; Lu, Y.; Zhang, H.; Liu, Z.; Huang, W. Flexible intelligent thermal management systems: sensing devices, signals, and applications. *Nano. Energy.* **2025**, *138*, 110842. DOI
57. Yao, Y.; Huang, Z.; Xie, P.; et al. Carbothermal shock synthesis of high-entropy-alloy nanoparticles. *Science* **2018**, *359*, 1489-94. DOI PubMed

Disclaimer/Publisher’s Note: All statements, opinions, and data contained in this publication are solely those of the individual author(s) and contributor(s) and do not necessarily reflect those of OAE and/or the editor(s). OAE and/or the editor(s) disclaim any responsibility for harm to persons or property resulting from the use of any ideas, methods, instructions, or products mentioned in the content.

© The Author(s) 2026. Open Access This article is licensed under a Creative Commons Attribution 4.0 International License (https://creativecommons.org/licenses/by/4.0/), which permits unrestricted use, sharing, adaptation, distribution and reproduction in any medium or format, for any purpose, even commercially, as long as you give appropriate credit to the original author(s) and the source, provide a link to the Creative Commons license, and indicate if changes were made.